Nano-Micro Letters
e-ISSN 2150-5551
CN 31-2103/TB
ARTICLE
https://doi.org/10.1007/s40820-026-02127-6

Cite as
Nano-Micro Lett.
(2026) 18:279

Received: 6 December 2025
Accepted: 3 February 2026

Polyphenol-Gated Composite Electrolytes with Enhanced Cross-Phase Lithium-Ion Transport for Solid-State Lithium Batteries

Xiaoxiao Li[1], Minqiang Jiang[1], Kai Chen[1], Zhixiang Cai[1], Yingxin Zhang[1], Jiamei Luo[1], Lei Hou[2], Yazhou Zhou[3], Chao Zhang[1], Hui Zhang[1] ✉, Feili Lai[4,5] ✉, Yue-E Miao[1] ✉, Tianxi Liu[1,6], Klaus Müllen[3,7]

HIGHLIGHTS

- A biomimetic polyphenol-gated strategy is proposed to promote interfacial Li^+ - selective transport in composite solid electrolytes by chemically bonding the polymer matrix and ceramic nanofibers.
- The polyphenol interlayers serve as the chemical gates with –OH and –NH groups to immobilize lithium salt anions and carbonyl groups to coordinate Li^+, thus lowering the energy barrier and promoting rapid Li^+ transport at interface.
- The assembled Li||$LiFePO_4$ batteries exhibits an impressive capacity of 151.6 mAh g^{-1} and long lifespan over 600 cycles.

Abstract Solid-state lithium (Li) batteries offer high-energy density and operational safety but face sluggish Li^+ transport in polymer/ceramic composite solid-state electrolytes. Herein, we propose a bioinspired polyphenol-gated interfacial engineering that mimics ion-selective protein channels to enhance Li^+-selective transport across the polymer–ceramic interface. Polyphenols such as polydopamine, poly-tannic acid, and poly-gallic acid chemically couple $La_{0.56}Li_{0.33}TiO_3$ ceramic nanofibers and glycidyl polyether matrix. Within this interface, carbonyl groups selectively coordinate Li^+ and facilitate directional migration. On the other hand, hydroxyl and amino groups immobilize anions via hydrogen bonding. This chemical gating nearly doubles interfacial Li^+ concentration and boosts transference number to 0.68. The corresponding Li||$LiFePO_4$ battery exhibits stable cycling over 600 cycles with 85.5% capacity retention at 1 C, while the pouch cell delivers reliable operation under mechanical stress caused by bending and puncturing. This work demonstrates that polyphenol-gated interfaces are essential for promoting selective and efficient cross-phase Li^+ transport for high-performance solid-state lithium-metal batteries.

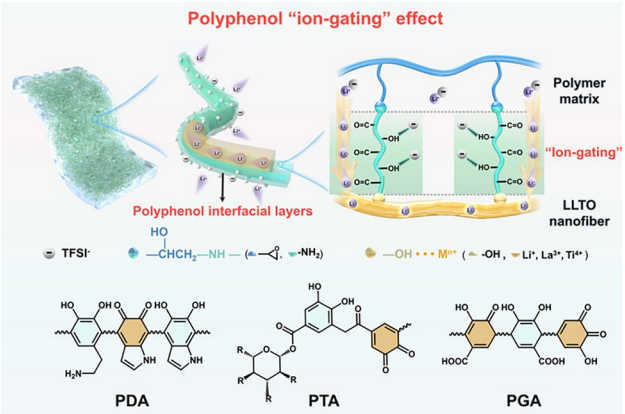

KEYWORDS Polyphenol-Gated Interface; Composite Solid-State electrolytes; Li^+- Selective Transport; Polymer-Ceramic Interface; Solid-State Lihium-Matel Batteries

✉ Hui Zhang, zhanghui@dhu.edu.cn; Feili Lai, feililai@sjtu.edu.cn; Yue-E Miao, yuee_miao@dhu.edu.cn
[1] State Key Laboratory of Advanced Fiber Materials, College of Materials Science and Engineering, Donghua University, 2999 North Renmin Road, Shanghai 201620, People's Republic of China
[2] State Key Laboratory of Advanced Fiber Materials, College of Chemistry and Chemical Engineering, Donghua University, 2999 North Renmin Road, Shanghai 201620, People's Republic of China
[3] Nanotechnology Centre, Centre for Energy and Environmental Technologies, VŠB-Technical University of Ostrava, 17. Listopadu 2172/15, 70800 Ostrava-Poruba, Czech Republic
[4] Department of Chemistry, KU Leuven, Celestijnenlaan 200F, 3001 Louvain, Belgium
[5] State Key Laboratory of Metal Matrix Composites, School of Materials Science and Engineering, Shanghai Jiao Tong University, Shanghai 200240, People's Republic of China
[6] Key Laboratory of Synthetic and Biological Colloids, Ministry of Education, School of Chemical and Material Engineering, Jiangnan University, Wuxi 214122, People's Republic of China
[7] Department of Molecular Spectroscopy, Max Planck Institute for Polymer Research, Ackermannweg 10, 55128 Mainz, Germany

Published online: 10 March 2026

1 Introduction

All-solid-state lithium-metal batteries (ASSLMBs) have emerged as next-generation energy storage technology that combines high-energy density and safety. Unlike traditional LMBs that use flammable liquid electrolytes, ASSLMBs employ solid-state electrolytes that suppress leakage, reduce thermal runaway risks, and enable stable operation of Li anodes [1–3]. As a critical component, the solid electrolyte significantly influences overall battery performance. Polymer/ceramic composite solid-state electrolytes (CSEs) represent a leading strategy in this field. These systems integrate the flexibility and processability of polymers with high ion conductivity of ceramic fillers. Common polymers include poly(ethylene oxide) (PEO), poly(vinylidene fluoride) (PVDF), polyacrylonitrile (PAN), while typical ceramic fillers are garnet-type $Li_7La_3Zr_2O_{12}$ (LLZO), $Li_{6.75}La_3Zr_{1.75}Ta_{0.25}O_{12}$ (LLZTO), and perovskite-type $La_{0.56}Li_{0.33}TiO_3$ (LLTO) [4]. However, the electrochemical performance of these CSEs is still limited by inefficient Li^+ transport across the polymer-ceramic interface.

To improve Li^+ transport in CSEs, various concepts have been developed which can be categorized primarily into two approaches: (1) Enhancing the distribution of ceramic fillers in the polymer matrix. Uniform dispersion of fillers is critical for establishing continuous Li^+-conducting networks and increasing the effective interfacial area for ion exchange. However, ceramic fillers often agglomerate. To address this issue, one method utilizes three-dimensional (3D) ceramic nanofiber frameworks (e.g., LLZO and LLTO) [5–8]. These frameworks provide interconnected ion pathways. However, the weak van der Waals forces at the polymer-ceramic interface limit ion exchange [9]. This reduces the local Li^+ concentration at the ceramic surface and undermines the contribution of the ceramic phase to overall conductivity [10]. (2) Reducing the interfacial resistance at polymer–ceramic contacts. Polymers (e.g., PEO and PVDF) conduct Li^+ primarily through segmental chain motion, while ceramics rely on vacancy-mediated lattice diffusion [11]. At the interface, Li^+ hopping across these heterogeneous phases creates energy barriers, and space-charge layers would further impede Li^+ transfer by establishing ion concentration gradients [12–14]. As a result, many CSEs exhibit low Li^+ transference numbers, often below 0.4 [15–19]. Various interfacial engineering approaches have been developed to mitigate these limitations. They include coatings with Li^+-conductive layers such as lithium phosphate [20], ionic liquids [21], silane coupling agents like 3-isocyanotopropyltriethoxytsilane [22], 3-methacryloxypropyltrimethoxysilane [23], and oxygen-rich polymer interlayers. Among them, polymer interlayers are particularly promising [24–26]. Polydopamine (PDA) is a notable example due to its strong interfacial adhesion and chemical reactivity [27, 28]. When grafted onto ceramic surfaces, these interlayers offer multiple functional groups (i.e., catechol, carbonyl, and hydroxyl) capable of interacting with both the polymer matrix and lithium ions and enabling enhanced ion conductivity [29–31]. While PDA has shown promise in improving filler dispersion and interfacial compatibility, most studies focus on macroscopic effects. The role of PDA in promoting selective Li^+ transport at the polymer–ceramic interface remains largely unexplored. Beyond improving physical contact, there is a critical need for molecular-level interfacial designs that facilitates directional Li^+ transfer and inhibits anion migration.

In biological systems, the cytomembrane containing channel proteins can control the migration of ions (like Na^+, K^+, or Ca^{2+}) in and out of the cell precisely (Fig. 1a). The narrow channels consisting of carbonyl groups form stable coordination with K^+ and allow the passage, while restricting that of other ions [32]. Inspired by this natural principle, we introduce polyphenols including PDA, polytannic acid (PTA), and poly-gallic acid (PGA) to build Li^+-selective transport channels across the polymer-ceramic interface (Fig. 1b). These interlayers serve as chemical gates in which carbonyl groups coordinate Li^+ to lower interfacial energy barrier, and –OH and –NH groups immobilize bis(trifluoromethanesulfonyl)imide ($TFSI^-$) anions via hydrogen bonding. This gating effect increases free Li^+ concentration at the interface and enhances selective cross-phase ion transport compared to systems without polyphenol modification. In practical devices, Li||$LiFePO_4$ cells with PDA-gated CSE exhibit excellent cycling stability over 1000 cycles at 5 C. The pouch cell achieves an initial capacity of 141.0 mAh g^{-1} with 82.9% retention after 400 cycles at 1 C. These results provide insight into regulating interfacial ion transport through molecular design of stable and high-rate solid-state lithium-metal batteries.

https://doi.org/10.1007/s40820-026-02127-6

2 Experimental Section

2.1 Materials

Lithium nitrate ($LiNO_3$), lanthanum nitrate hexahydrate ($La(NO_3)_3.6H_2O$), titanium (IV) butoxide titanate, lithium bis (trifluoromethanesulphony) imide (LiTFSI), 2,2-azobis (2-methylpropionitrile) (AIBN), and poly (ethylene glycol) dimethyl ether (PEGDE, $M_w = 500$) were purchased from Adamas-beta, polyvinyl pyrrolidone (PVP, $M_w = 1{,}300{,}000$) and tannic acid (TA) were got from Sigma-Aldrich, and acetic acid, N,N-dimethylformamide (DMF), 1-meathyl-2-pyrrolidinone (NMP), poly (ethylene glycol) methyl ether acrylate (PEGMA, $M_w = 480$), polyethyleneimine (PEI, $M_w = 400$), dopamine hydrochloride (DA), gallic acid (GA), and glycidyl methacrylate (GMA) were purchased from Aladdin. Polyvinylidene difluoride (PVDF, HSV900) was bought from Dongguan west plastic trade Co., Ltd. Active materials $LiFePO_4$ (LFP) and $LiNi_{0.8}Co_{0.1}Mn_{0.1}O_2$ (NCM811) were provided by Shenzhen Kejingstar (MTI) Technology Co., Ltd. And carbon black was purchased by Suzhou Sinero Technology Co., Ltd.

2.2 Preparation of the $La_{0.56}Li_{0.33}TiO_3$ (LLTO) Ceramic Nanofiber Electrolyte

The LLTO ceramic nanofiber electrolyte was prepared by electrospinning followed by high-temperature sintering method. Briefly, 0.262 g $LiNO_3$, 2.425 g $La(NO_3)_3.6H_2O$, and 3.403 g titanium (IV) butoxide titanate were added into 16 g DMF solvent with 16 wt% PVP and 13 wt% acetic acid. The mixture was stirred for 12 h to obtain a yellow transparent solution. The solution was then transferred into a 10 mL syringe and electrospun for 10 h to obtain the LLTO membrane precursor, named as p-LLTO. The electrospinning parameters were set as follows: the needle-to-collector distance was 15 cm, the injection speed was 0.08 mm min^{-1}, and the applied voltage was 15 kV. The p-LLTO was then transferred to an alumina boat and subjected to a segmented sintering process: calcination at 600 °C for 1 h with a heating rate of 2 °C min^{-1}, followed by annealing at 800 °C for 2 h in air to obtain the final LLTO ceramic nanofibers. Finally, the LLTO membranes were cut into 16-mm slice for battery assembly.

2.3 Preparation of Polyphenol-Modified LLTO Ceramic Nanofiber Electrolytes

DA (2 mg mL^{-1}) and PEI (2 mg mL^{-1}) were dissolved in 40 mL Tris buffer (pH = 8.5). Then, the LLTO nanofiber membrane was immersed in the above solution and placed in the dark for 12 h at room temperature. The modified LLTO membrane, signed as PDA_2@LLTO, was then rinsed 3 times with ultrapure water and dried in an oven at 80 °C for 24 h. Similarly, $PDA_{0.5}$@LLTO and PDA_4@LLTO were also prepared using the same method with the DA concentrations of 0.5 and 4 mg mL^{-1}, respectively.

Additionally, PTA_2@LLTO and PGA_2@LLTO membranes were synthesized using the same method with reactive monomer of TA and GA.

2.4 Preparation of Composite Solid-State Electrolytes

GMA monomers (1 g), PEGMA monomers (2 g), PEGDE (0.3 g), AIBN thermal initiator (0.03 g), and LiFTSI (0.66 g) were mixed and stirred for 2 h to obtain a homogeneous glycidyl polyether (GE) precursor solution. Subsequently, the precursor solution (60 μL) was dropped onto the prepared PDA_x@LLTO membrane and polymerized at 65 °C for 3 h. The final composite solid-state electrolyte, donated as PDA_x@LLTO/GE, was obtained after heating for additional 1 h at 100 °C to form the chemical bonding between the polyphenol layer and GE matrix. All steps and subsequent battery assembling were carried out in an argon-filled glovebox ($O_2 < 0.01$ ppm, $H_2O < 0.01$ ppm). PTA_2@LLTO/GE and PGA_2@LLTO/GE electrolytes were prepared using the same method.

2.5 Preparation of the Cathodes

LFP, super P, and PVDF with the mass ratio of 7:2:1 was mixed in NMP to form a uniform slurry of 10% solid content. Then, the slurry was coated on a carbon-coated aluminum foil and dried in a vacuum oven at 80 °C for 2 days to completely remove the solvent. And the dried electrode was then cut into a 12 mm disk with a mass loading of about 1 ~ 1.4 mg cm^{-2}. For the high LFP loading cathode, the areal loading of LFP was controlled at 5.0 mg cm^{-2}. The NCM811 cathode was prepared by the same method using a mixture

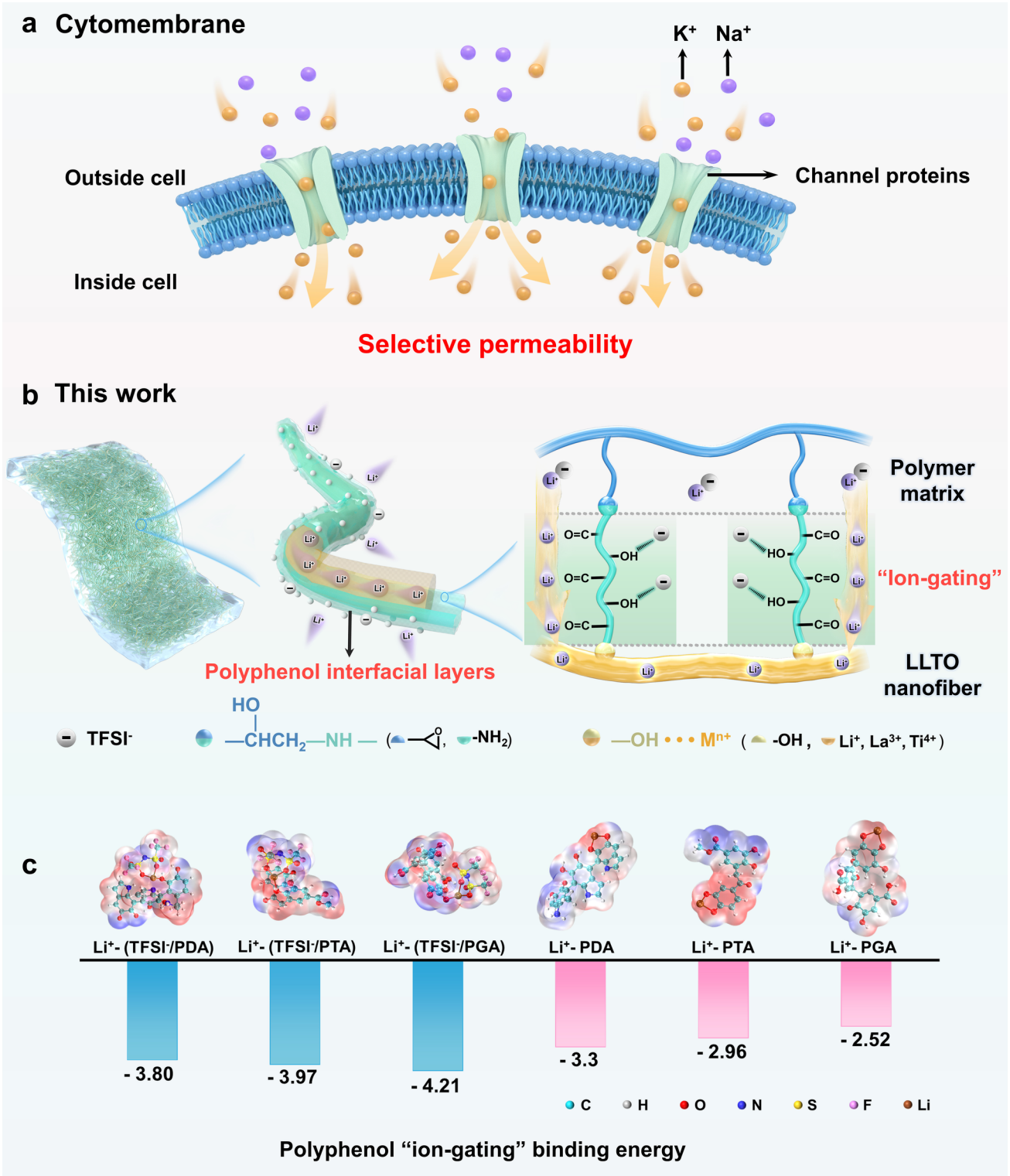

Fig. 1 Design of bioinspired ion-selective interface and Density Functional Theory (DFT) calculations of polyphenol interface. **a** Schematic illustration of selective permeability through cytomembranes. **b** Illustration of the polyphenol-gated interfacing, highlighting the chemical binding and bionic "ion-gating" effect at the inorganic-polymer interface. **c** Binding energies and electrostatic potential calculations of Li^+-$TFSI^-$ complexes at PDA, PTA, and PGA interfaces, including Li^+-C=O coordination strengths

https://doi.org/10.1007/s40820-026-02127-6

of NCM811, super P, and PVDF binder solution in NMP at a mass ratio of 8:1:1, and the corresponding active material loading was 1 mg cm^{-2}.

2.6 Materials Characterizations

The microstructure of the samples was characterized by field-emission electron microscope (FESEM, JSM 7500 F). Transmission electron microscope (TEM, Talos F200S) was used to analyze the morphology LLTO ceramic nanofibers before and after modifying with polyphenol layer, and energy-dispersive spectrometer (EDS) was used to map the surface element distribution. The crystal structure of LLTO was confirmed by X-ray diffraction (XRD, Bruker AXS D2 Phaser). Fourier transform infrared (FI-IR, Nicolet 6700) spectra and X-ray photoelectron spectroscopy (XPS, Thermo Scientific ESCALAB 250Xi equipped with Al, K_α X-ray source) spectra were conducted to characterize the chemical interactions between PDA and the LLTO nanofibers and polymer matrix. ^{7}Li solid-state nuclear magnetic resonance (NMR) and temperature-variable FTIR spectra results were collected by Bruker Avance 400 and Nicolet iS50 FTIR to investigate the distribution state of Li^+ in the CPEs and the Li^+ transport behavior at the polyphenol interfaces. Raman spectroscopy was carried out with Renishaw in Via-Reflex (532 nm). The mechanical properties were tested using the tensile machine (UTM2103, Shenzhen suns technology CO., Ltd.). The thermodynamic behavior was studied by differential scanning calorimetry (DSC, PerkinElmer DSC4000). The thermogravimetric analysis (TGA, NETZSCH TG 209F1 Libra) was measured under N_2 atmosphere to study the thermostability of the electrolytes.

2.7 Electrochemical Measurements

All electrochemical properties were performed using CR2025 coin cells. A CHI760E electrochemical workstation was employed to measure the electrochemical impedance spectroscopy (EIS), electrochemical window, and chronoamperometry spectra. All the electrochemical properties of the electrolytes, such as galvanostatic discharge/charge profiles, long cycling stability, and rate capability, were conducted at 60 °C using a LAND test system.

The impedance of the electrolytes was measured by EIS test in a frequency range from 100 kHz to 0.1 Hz. And the ionic conductivity was obtained from the symmetric cell assembled with two stainless steels and calculated using the following equation:

$$\sigma = \frac{L}{R \times S} \tag{1}$$

where σ is ionic conductivity, L is the thickness of the electrolyte, R is the impedance, and S is the contact area between the electrolyte and the stainless steel.

The activation energy (E_a) of the electrolytes was calculated using the Arrhenius equation:

$$\sigma = \mathrm{A}e^{\frac{-\mathrm{Ea}}{\mathrm{RT}}} \tag{2}$$

where A is the pre-exponential factor, R is the molar gas constant (8.314 J mol^{-1} K^{-1}), and T is the absolute temperature.

The Li^+ transference number ($t_{Li}{}^+$) of electrolytes was measured using a symmetric Li||Li cell with a chronoamperometry test under a DC voltage amplitude of 10 mV at room temperature. And the impedances before and after polarization were also measured by EIS. The $t_{Li}{}^+$ can be calculated according to Eq. (3):

$$t_{\mathrm{Li}}^{+} = \frac{I_s(\Delta \mathrm{V} - \mathrm{R}_0 I_0)}{I_0(\Delta \mathrm{V} - \mathrm{R}_s I_s)} \tag{3}$$

where I_0 and I_s are the initial and steady-state DC currents, R_0 and R_s are the interfacial impedances before and after polarization, and ΔV is the applied voltage (10 mV).

The electrochemical window stability of the electrolytes was evaluated by LSV using a Li||SS half-cell at a scan rate of 0.1 mV s^{-1} at room temperature. Galvanostatic cycling tests were conducted on LFP||Li full cells within a voltage range of 2.4–4.2 V.

2.8 Simulation Methods

2.8.1 Density Functional Theory (DFT) Calculations

DFT calculations and electrostatic potentials (ESP) were carried out by the Central Laboratory, School of Chemical and Material Engineering, Jiangnan University, to investigate the interactions between Li^+, $TFSI^-$, PDA, PTA, and PGA. All calculations were performed using the Gaussian 16 software

package. The B3LYP functional was adopted for all calculations in combination with the D3BJ dispersion correction. In geometry optimization and frequency calculations, the 6-31G(d,p) basis set was used. The singlet point energy calculations were performed with a larger basis set combination, in which the ma-def2-TZVP basis set was used. The optimized structures were used to calculate the ESP and adsorption energies. The most negative regions in the ESP were identified as the adsorption sites for lithium-ion. Therefore, the binding energy ($E(\mathrm{AB})_{\mathrm{Binding}}$) was calculated using Eq. (4):

$$E(\mathrm{AB})_{\mathrm{Binding}} = E(\mathrm{AB}) - E(A) - E(B) \quad (4)$$

where $E(\mathrm{AB})$, $E(A)$, and $E(B)$ represent the single-point energy of complex AB, component A, and component B, respectively.

2.8.2 Molecular Dynamics (MD) Simulations

MD simulations were performed using the GROMACS package to probe Li^+ transport across the LLTO/polymer interface at the atomic level in LLTO/GE and PDA_2@LLTO/GE systems. The initial configurations for the two systems were constructed using PACKMOL software. The parameter fitting was performed via the density functional theory (DFT) package Orca, using the B3LYP exchange–correlation functional supplemented with Grimme's DFT-D3(BJ) empirical dispersion correction. For all species in this work, the RESP2(0.5) charges (combining gas-phase and implicit solvent (SMD model) liquid-phase charge distributions) were calculated using Orca and the Multiwfn package, and this non-bonded force field charge model was adopted for subsequent MD simulations.

The MD simulation was first performed in the NVT ensemble at 298 K with a 1 fs time step for 1 ns. Then, the equilibrium simulation was conducted in the NPT ensemble (1 bar, 298 K) in a cubic box (periodic boundary conditions applied in all directions) with a 1 fs time step for 2 ns. Finally, the production simulation was carried out in the NVT ensemble at 298 K with a 1 fs time step for 1 ns. Radial distribution functions (RDF, $g_{ij}(r)$) and coordination numbers (CN, N_i) are computed as:

$$N_i = 4\pi n_j \int_0^{R_M} g_{ij}(r) r^2 dr \quad (5)$$

where R_M corresponds to the distance of the first minimum after the first peak in the $g_{ij}(r)$. All the system visualizations of MD simulations are rendered by VMD software. The mean square displacement (MSD) of Li^+ is calculated by the Einstein equation:

$$\mathrm{MSD} = < [R(t) - R(0)]^2 > \quad (6)$$

in which $R(t)$ and $R(0)$ are the positions of the Li^+ atoms at time t and 0. And the diffusion constant (D) is the slope of MSD versus time with a factor of 1/6:

$$D = \frac{1}{6} \lim_{t \to \infty} \frac{\mathrm{d}}{\mathrm{d}t} \mathrm{MSD} \quad (7)$$

3 Results and Discussion

3.1 Bioinspired Ion-Selective Interfaces Design and Structural Characterizations of Polyphenol-Gated CSEs

As a molecular basis for "ion-gating" effect, we performed density functional theory (DFT) calculations to assess the interactions between lithium salts and polyphenol layers (Fig. 1c). The results show that $TFSI^-$ anions form stable hydrogen bonds with –OH and –NH groups in all three polyphenols, as indicated by the negative binding energy (ΔE) (Fig. S1). These anion-specific interactions immobilize $TFSI^-$ at the interface and weaken its coordination with Li^+. To quantify this effect, we examined ternary complexes consisting of Li^+, $TFSI^-$, and polyphenol molecules. Compared to the strong Li^+-$TFSI^-$ binding energy of – 6.39 eV (Fig. S2a), the ternary complexes Li^+-$TFSI^-$/PDA (– 3.80 eV), Li^+-$TFSI^-$/PTA (– 3.97 eV), and Li^+-$TFSI^-$/PGA (– 4.21 eV) display significantly reduced binding energies (Fig. 1c). This reduction suggests that polyphenol participates in the solvation structure and promotes lithium salt dissociation, thereby enriching the interfacial region with mobile Li^+ ions. Electrostatic potential (ESP) analysis supports this observation. While Li^+ exhibits a highly localized positive field potential when bound to $TFSI^-$ alone (Fig. S2b), its ESP distribution becomes more diffuse in polyphenol-containing complexes. This shift indicates a weakened Li^+–$TFSI^-$ interaction and a higher local concentration of Li^+ at the interface. Moreover, carbonyl groups in the polyphenol backbones provide additional coordination sites for Li^+.

https://doi.org/10.1007/s40820-026-02127-6

The calculated ΔE of Li^+ with these carbonyl groups are − 3.30 eV (PDA), − 2.52 eV (PGA), and − 2.96 eV (PTA). This suggests strong ion–dipole interactions that facilitate directional Li^+ migration. Altogether, these theoretical findings verify that polyphenol interlayers can act as ion-selective gates to facilitate Li^+ transport into the ceramic phase.

We selected PDA-gated CSEs as a representative system to demonstrate our fabrication protocol which is illustrated in Fig. S3. A freestanding $La_{0.56}Li_{0.33}TiO_3$ (LLTO) nanofiber membrane was first formed via electrospinning followed by solid-state sintering. The resulting LLTO nanofibers exhibit porous, grain-connected structures with a diameter of ~ 300 nm, as confirmed by scanning electron microscopy (SEM) and transmission electron microscope (TEM) (Figs. S4, S5). To introduce the "ion-gating" layer, a mussel-like- PDA coating was then deposited on the LLTO surface (diameter: 16 mm, thickness ~ 150 μm). The PDA-coated LLTO, denoted PDA_x@LLTO (dopamine concentration x = 0.5, 2, and 4 mg mL^{-1}) exhibits a uniform surface coverage, as visualized by SEM images compared to bare LLTO nanofibers (Figs. 2a andS6). TEM images (Figs. 2b and S7) reveal a conformal PDA coating on LLTO nanofibers with thicknesses of approximately 10, 18, and 29 nm for $PDA_{0.5}$@LLTO, PDA_2@LLTO, and PDA_4@LLTO, respectively. Elemental mappings confirm the homogeneous distribution of C and N elements and verify the successful PDA functionalization (Fig. 2c). X-ray diffraction (XRD) patterns (Fig. S8) demonstrate that the crystalline structure of LLTO remains intact after PDA coating. X-ray photoelectron spectroscopy (XPS) analysis was carried out to investigate the chemical interactions at the interface. In the Ti 2*p* spectrum (Fig. 2d), PDA_2@LLTO exhibits shifted Ti–O peaks along with new signals at 456.7 and 461.5 eV. This can be attributed to Ti–N bonds formed between Ti^{4+} in LLTO and amine groups in PDA. Additional evidence of La–N bond formation (Fig. S9) supports the strong interfacial coordination between the PDA layer and the LLTO surface.

Subsequently, glycidyl polyether (GE) was infiltrated into the coated nanofiber scaffold via thermopolymerization of glycidyl methacrylate and poly(ethylene glycol) methyl ether acrylate. This flexible, integrated CSE membrane is denoted as PDA_x@LLTO/GE. The PDA_2@LLTO/GE membrane exhibits a uniform thickness of ~ 325 μm and excellent flexibility (Fig. 2e). Thermogravimetric analysis (Fig. S10) indicates that the inorganic LLTO content in the final membrane is approximately 20 wt%, which is significantly higher than the typical filler limit (~ 10 wt%) in conventional inorganic nanoparticles (such as LLZTO)-based CSEs [33]. This increased loading originates from the continuous fibrous framework, which effectively mitigates filler agglomeration and ensures uniform phase dispersion within the polymer matrix. Fourier transform infrared (FTIR) spectroscopy (Fig. 2f) exhibits the weakened epoxy peak at 910 cm^{-1} in PDA_2@LLTO/GE compared to GE and reveals the ring-opening reaction of GE's epoxy groups induced by amino groups in PDA. The enhanced C–O–C stretching peak (~ 1108 cm^{-1}) is in accord with structural rearrangements in the GE network upon interaction with PDA. Altogether, these results indicate strong interaction between PDA and the polymer matrix. Differential scanning calorimetry (DSC) curves show a slightly increased glass transition temperature (T_g) and reflect an altered polymer chain mobility due to interfacial interactions (Fig. S11). Adhesion tests demonstrate strong contact with Li metal (80 N m^{-1} adhesion energy, Fig. S12), and the tensile strength of PDA_2@LLTO/GE is four times higher than that of unmodified the LLTO/GE membrane (Fig. 2g). These results confirm the successful construction of a homogeneous, chemically integrated PDA interlayer that bridges polymer and ceramic phases (Fig. 2h), which reinforces the structural integrity of the composite electrolyte. Besides, endowed with abundant functional groups, this structurally robust PDA interlayer underpins the subsequent formation of the ion-selective interface, enabling enhanced solid-state lithium transport. To demonstrate the general applicability of the polyphenol-gated interfacial design, PTA_2@LLTO and PGA_2@LLTO were also synthesized using the same method. SEM analysis (Fig. S13) confirms successful polymer coating and supports the structural foundation for Li^+-selective interface across different polyphenol systems.

3.2 Exploring the Ion Transport Properties and "Ion-Gating" Mechanism in Polyphenol-Gated CSEs

We next evaluated the ion transport performance of polyphenol-gated CSEs. According to electrochemical impedance spectroscopy (EIS, Fig. S14), the PDA_2@LLTO/GE

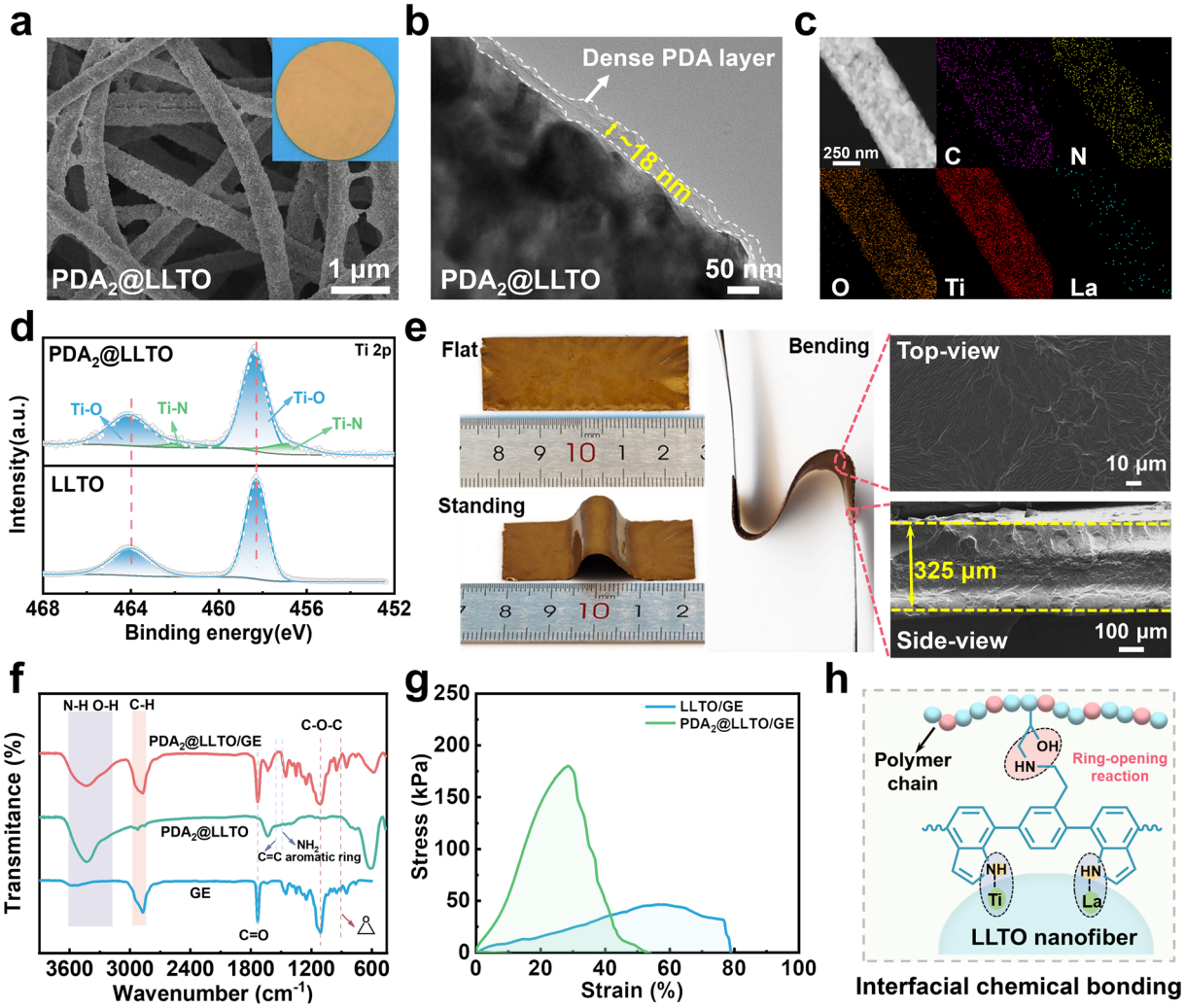

Fig. 2 Synthesis and characterization of PDA_2@LLTO/GE electrolyte. **a** SEM, **b** TME images, and **c** corresponding EDS elemental mappings of PDA_2@LLTO nanofibers. **d** Ti 2*p* XPS spectra of LLTO and PDA_2@LLTO membranes. **e** Photographs of PDA_2@LLTO/GEs showing its flexibility, inset: top-view and side-view morphology. **f** FTIR spectra of GE, PDA_2@LLTO, and PDA_2@LLTO/GE electrolytes. **g** Tensile stress–strain curves of LLTO/GE and PDA_2@LLTO/GE electrolytes. **h** Schematic of interfacial chemical bonding between the PDA interlayer, GE matrix, and LLTO nanofibers

electrolyte delivers a high ion conductivity (σ) of 3.01×10^{-4} S cm^{-1} at 60 °C, more than four times higher than that of LLTO/GE (7.12×10^{-5} S cm^{-1}). This improvement was further analyzed through temperature (*T*)-dependent conductivity measurements. From the Arrhenius plots (σ vs. T, – 10 to 60 °C), the activation energy (E_a) for Li^+ transport in PDA_2@LLTO/GE was calculated to be 0.57 eV, lower than the value of 0.64 eV for LLTO/GE (Fig. 3a): there is enhanced Li^+ migration across the interface in the PDA-gated system. Additionally, the influence of PDA thickness on the ionic conductivity was further investigated. As shown in Fig. S15, a thin PDA layer is discontinuous, failing to fully eliminate the interfacial voids at the GE matrix and LLTO filler. Notably, an over-thick layer will deteriorate the Li^+ migration due to the prolonged interfacial ion transport pathway caused by the intrinsically low ion conduction of PDA barrier. Therefore, the optimized PDA_2@LLTO/GE achieves highest room-temperature ionic conductivity of 3.57×10^{-5} S cm^{-1}. In terms of electrochemical stability, linear sweep voltammetry (LSV) shows that the PDA_2@LLTO/GE electrolyte possesses an extended electrochemical window of up to 5.05 V versus Li/Li^+, compared to that of LLTO/GE (Fig. S16). This broader voltage range indicates improved oxidative stability and suggests better

 https://doi.org/10.1007/s40820-026-02127-6

compatibility at the electrolyte–electrode interface. Moreover, the Li^+ transference number (t_{Li}^+) increases from 0.39 in LLTO/GE to 0.68 in PDA_2@LLTO/GE at 60 °C. This can be attributed to effective immobilization of $TFSI^-$ by the polar groups of PDA (Fig. S17). We evaluated two additional polyphenol-modified CSEs, namely PTA_2@LLTO/GE and PGA_2@LLTO/GE, to verify the general applicability. These systems achieve improved room-temperature ion conductivities of 2.79×10^{-5} and 2.61×10^{-5} S cm^{-1} as compared to that of LLTO/GE (1.17×10^{-5} S cm^{-1}). Their t_{Li}^+ also increases to 0.58 (PTA) and 0.53 (PGA), respectively (Figs. S18 and S19). The observed differences in ionic conductivity and t_{Li}^+ among the three polyphenol interfaces likely stem from the limited functional groups within PTA (–OH) and PGA (–COOH), whereas the PDA features more abundant functional polar groups (–OH, –NH), thereby enabling the PDA_2@LLTO/GE to deliver the optimal ion transport kinetics. Besides, these values compare favorably with previously reported polymer-ceramic CSE systems (Fig. 3b) such as $Li_{1.3}Al_{0.3}Ti_{1.7}(PO_4)_3$/poly (vinylidene fluoride-hexa-fluoropropylene) (LATP/PVDF-HFP) and β-cyclodextrin modified

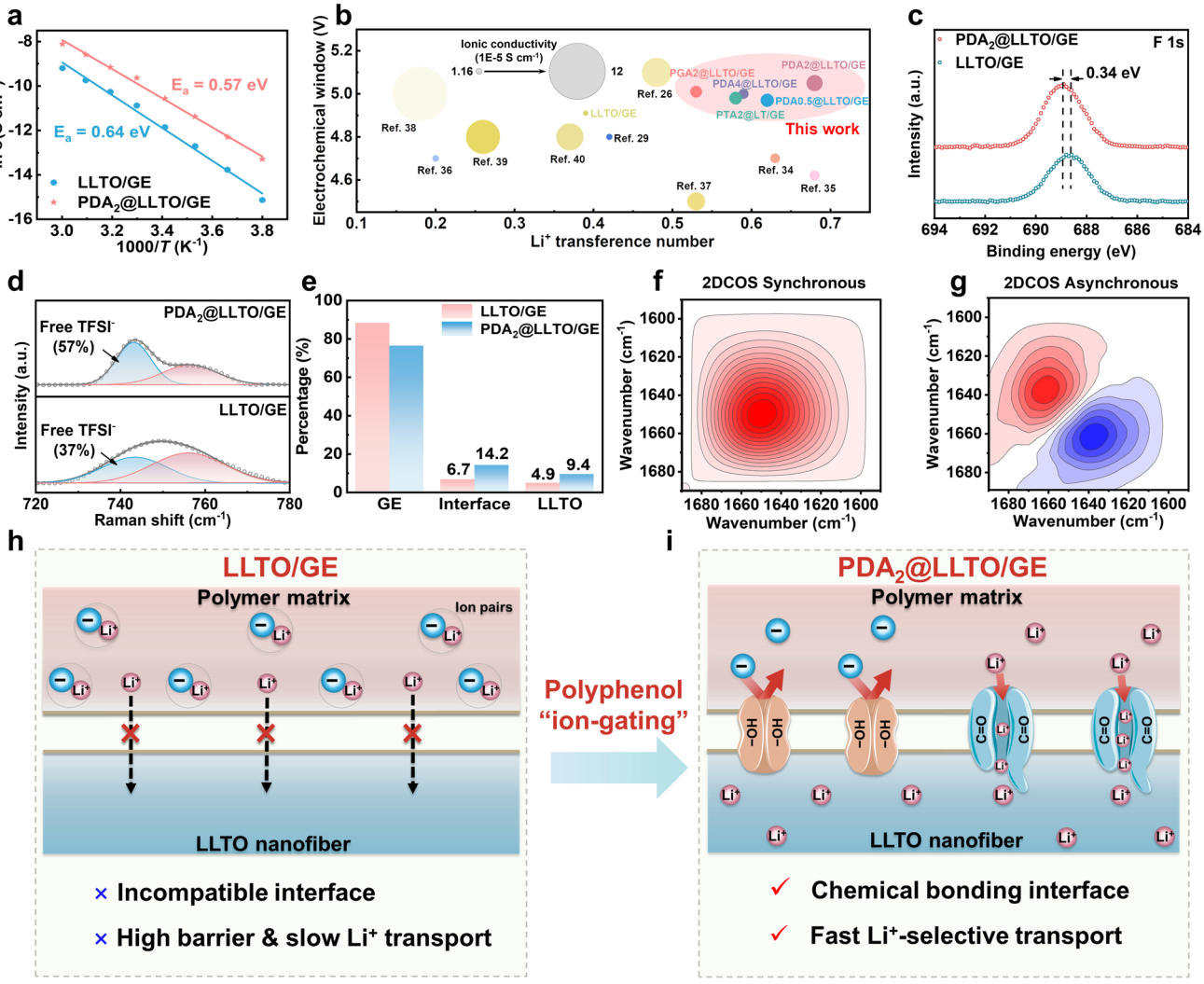

Fig. 3 Electrochemical performance of PDA_2@LLTO/GE electrolyte and Li^+-transport mechanism at polyphenol interface. **a** Arrhenius plots of ion conductivities (σ) of LLTO/GE and PDA_2@LLTO/GE electrolytes. **b** Comparison of σ, t_{Li}^+ and electrochemical windows for various reported CSEs at room temperature (The circle size represents σ). **c** F 1*s* XPS spectra, and **d** Raman spectra of LLTO/GE and PDA_2@LLTO/GE electrolytes. **e** Quantitative Li^+ distribution in LLTO/GE and PDA_2@LLTO/GE electrolytes derived from solid-state ^7Li NMR spectra. **f** Synchronous, and **g** asynchronous 2DCOS spectra of PDA_2@LLTO/GE electrolyte (red: positive; blue: negative intensities). **h, i** Schematic illustration of Li^+ transport pathways at the organic–inorganic interface in LLTO/GE and PDA_2@LLTO/GE, respectively

LLZTO/PEO that typically display small t_{Li^+} (< 0.5), lower conductivity, and limited stability [26, 29, 34–40].

To gain insights into Li^+ transport enhancement across at the polyphenol-gated interface, we employed multiple analytic techniques. XPS was performed to assess the interaction between Li^+ and $TFSI^-$ in the CSEs (Fig. 3c). The F 1*s* peak of $TFSI^-$ shifts from 688.64 eV in LLTO/GE to 688.90 eV in PDA_2@LLTO/GE, indicating improved interaction between $TFSI^-$ and the polar groups in PDA, which weaken Li^+-$TFSI^-$ binding and promote salt dissociation. Raman analysis supports this result (Fig. 3d). The free $TFSI^-$ peak at 743 cm^{-1} becomes more intense in PDA_2@LLTO/GE, while the undissociated in LLTO/GE shifts slightly [41]. The fraction of free $TFSI^-$ increases by ~ 20%, implying higher Li^+ availability for conduction. Solid-state ^7Li magic-angle spinning nuclear magnetic resonance (MAS NMR) reveals changes in Li^+ distribution in different environments. In pure LLTO nanofibers, broad ^7Li signals appear at 1.23 and 2.95 ppm. In contrast, GE shows narrowed peaks at 0.64 and 0.97 ppm (Fig. S20a), suggesting restricted Li^+ mobility in the polymer matrix. In LLTO/GE, deconvoluted peaks disclose Li^+ populations in the GE matrix (88.4%), LLTO nanofibers (4.9%), and GE-LLTO interface (6.7%). In PDA_2@LLTO/GE, the Li^+ content at the inorganic phase and PDA-LLTO interface increases to 9.4% and 14.2%, respectively (Figs. 3e and S20b, c). This indicates enhanced Li^+ exchange across the interface. Accordingly, the PDA interlayer effectively promotes interfacial Li^+ transport and strengthens the contribution of the 3D ceramic network to overall ion conductivity.

To study the interaction between Li^+ and carbonyl functional groups at different temperatures, we recorded temperature-dependent FTIR spectra. In PDA_2@LLTO/GE, the C=O···H band at 1648 cm^{-1} and C=O···Li^+ at 1629 cm^{-1} both shift to lower wavenumbers as the temperature increases from 30 to 100 °C, accompanied by a decrease in peak intensity (Fig. S21a) [42]. This behavior suggests enhanced Li^+-carbonyl interaction at elevated temperatures, indicating stronger coordination upon heating [43]. Two-dimensional correlation spectroscopy (2DCOS), including synchronous and asynchronous spectra, was employed to analyze the thermal changes of hydrogen-binding and lithium-binding carbonyl (Fig. 3f, g). According to Noda's rule and the temperature-variable FTIR results [44, 45], three characteristic carbonyl modes were identified: 1668 cm^{-1} (C=O in dipole–dipole, C=O···C = O), 1648 cm^{-1} (C=O in hydrogen bonding, C=O···H), and 1629 cm^{-1} (C=O in Li^+ coordination, C=O···Li^+), as summarized in Table S1. The order of these modes under thermal excitation reveals a strong C=O···Li^+ interaction (Fig. S23), which supports its key role in facilitating Li^+ conduction. Compared to the poorly matched interface in the LLTO/GE case (Fig. 3h), the PDA interlayer achieves an "ion-gating" effect that promotes fast, Li^+-selective transport across the organic–inorganic interface (Fig. 3i). Similar 2DCOS trends in PTA_2@LLTO/GE and PGA_2@LLTO/GE confirm the carbonyl-mediated Li^+ transport as a key mechanism in polyphenol-gated CSEs (Figs. S21b, c and S22).

Molecular dynamic (MD) simulations were performed to visualize ion solvation environments. In the LLTO/GE system, time-resolved snapshots (Fig. 4a) show that Li^+ ions remain closely coordinated with $TFSI^-$ anions which indicates limited dissociation. In contrast, PDA_2@LLTO/GE exhibits a disrupted Li^+–$TFSI^-$coordination structure and a higher concentration of free Li^+ close to the interface (Fig. 4b). This observation is supported by an analysis of radial distribution functions (RDF). In both systems, the Li^+–O ($TFSI^-$) peak appears at 0.21 Å, reflecting initial ion pairing. However, the Li^+–O (GE) peak shifts from 0.22 Å in LLTO/GE (Fig. 4c) to 0.20 Å in PDA_2@LLTO/GE (Fig. 4d), along with an increase in intensity. This observation suggests stronger Li^+ interactions with the polymer matrix and reduced association with $TFSI^-$ in PDA_2@LLTO/GE. In addition, a new peak at 0.21 Å, corresponding to Li^+–O (PDA), confirms that the PDA interlayer contributes directly to Li^+ coordination in an additional transport mechanism: the PDA layer introduces C=O groups that coordinate with Li^+. At the same time, –OH and –NH groups stabilize $TFSI^-$ through hydrogen bonding. Together, these interactions promote lithium salt dissociation and create additional pathways for Li^+ migration. Mean-square displacement (MSD) analysis confirms the enhanced ion mobility. Li^+ diffusion coefficient in PDA_2@LLTO/GE reaches 3.50×10^{-9} cm^2 S^{-1}, significantly higher than 1.11×10^{-9} cm^2 S^{-1} in LLTO/GE (Fig. 4e).

3.3 Electrochemical Stability of the Li Symmetric Cells

Li symmetric batteries were assembled to assess the performance of PDA_2@LLTO/GE electrolyte in the long Li plating/stripping process. The Li| PDA_2@LLTO/GE |Li cell

https://doi.org/10.1007/s40820-026-02127-6

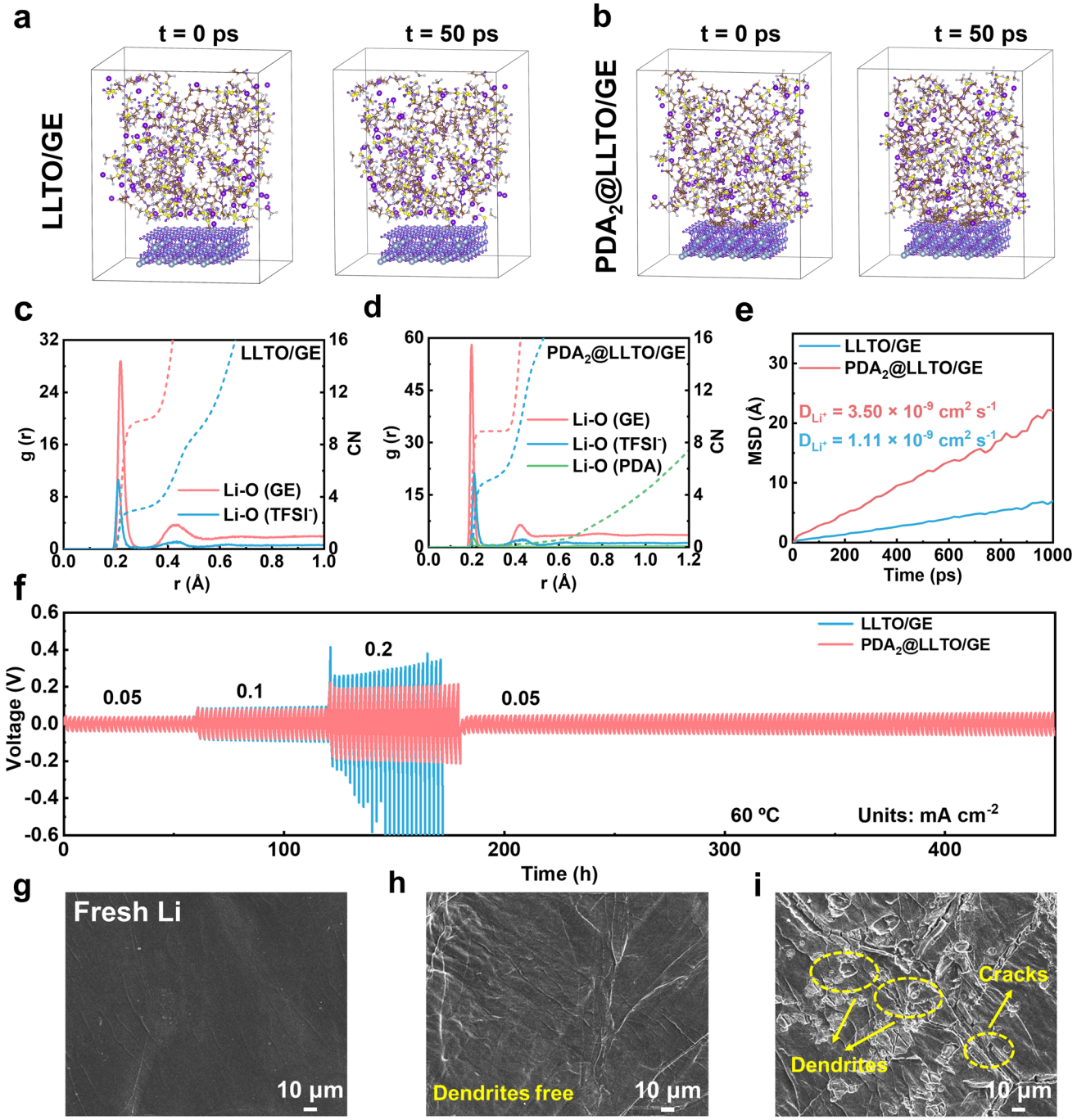

Fig. 4 Molecular dynamics (MD) simulation and Li||Li symmetric cell performance of PDA_2@LLTO/GE electrolyte. MD snapshots of **a** LLTO/GE and **b** PDA_2@LLTO/GE at different time intervals. RDFs (solid line) and coordination numbers (dashed line) of Li–O pairs in **c** LLTO/GE and **d** PDA_2@LLTO/GE. **e** Mean squared displacement (MSD) profiles of Li^+ in LLTO/GE and PDA_2@LLTO/GE. **f** Rate performance of symmetric cells using two electrolytes at different current density at 60 °C. SEM images of **g** fresh Li foil, and 100-cycled Li anode at 0.1 mA cm^{-2} in **h** Li| PDA_2@LLTO/GE |Li and **i** Li| LLTO/GE |Li symmetric batteries

exhibits stable cycling for over 1600 h at 0.1 mA cm^{-2} with a low and consistent polarization voltage below 200 mV (Fig. S24). In contrast, the Li| LLTO/GE |Li cell shows a rapid increase in overpotential and fails after 350 h. This is likely due to severe side reactions stemming from poor interfacial ion transport. Furthermore, the lithium dendrite suppression capability was also evaluated. The PDA_2@LLTO/GE endows the symmetric cell to reach a critical current density (CCD) of 0.6 mA cm^{-2}, while the Li| LLTO/GE |Li cell exhibits a much lower value of 0.3 mA cm^{-2} (Fig. S25). Therefore, the PDA-modified CSE displays enhanced dendrite suppression under high-current density, which contributes to the stable and long-term cycling performance. The reversible rate capability was further evaluated by increasing the current density from 0.05 to 0.2 mA cm^{-2} (Fig. 4f). The Li| PDA_2@LLTO/GE |Li cell maintains a stable polarization voltage across all current densities and shows a reversible behavior when the current returns to 0.05 mA cm^{-2}. In comparison, the LLTO/GE-based cell exhibits severe voltage fluctuations under 0.2 mA cm^{-2}. Throughout the tests, PDA_2@LLTO/GE-based cell consistently exhibits lower polarization than LLTO/GE-based cell at all current densities (Fig. S26). This confirms enhanced ion transport enabled by the PDA-gated ion-selective interface. SEM images of cycled Li anodes show distinct surface differences. The Li anode with PDA_2@LLTO/GE remains flat and smooth, with no visible dendrite formation after 100 cycles (Fig. 4g, h), whereas obvious cracks and dendrites are observed for the LLTO/GE system (Fig. 4i). These results underscore the power of a PDA-gated interface in promoting uniform Li^+ flux and suppressing dendrite growth through fast cross-phase conduction pathways.

The influence of PDA_2@LLTO/GE on the formation of the solid electrolyte interphase (SEI) plays a critical role in governing Li deposition behavior and overall battery performance. The C 1*s* XPS spectra show stronger signals for C–C (284.8 eV) and C=O (286.5 eV) in PDA_2@LLTO/GE than in LLTO/GE (Fig. 5a) which is evidence of a more flexible, organo-rich SEI layer that suppresses Li corrosion [46]. The S 2*p* spectra exhibit two characteristic peaks at 170.0 and 168.7 eV, which can be assigned to sulfate groups from LiTFSI decomposition (Fig. S27a). This decomposition contributes to an electrically insulating layer. Stronger signals of Li_3N (Fig. 5b) and LiF (Fig. 5c) are observed in PDA_2@LLTO/GE which are known to facilitate Li^+ transport across CSE-Li anode interface (Fig. S27b) [47]. Quantitative analysis confirms a reduced proportion of poorly conductive Li_2CO_3 and increased content of LiF and Li_3N in PDA_2@LLTO/GE compared to LLTO/GE (Fig. 5d). Furthermore, to evaluate the cycling stability of the PDA_2@LLTO/GE electrolyte, the depth-resolved XPS spectra were performed to investigate the SEI compositions on Li anodes after 100 cycles at a higher density current of 0.2 mA cm^{-2}. As shown in Fig. S28a, with the increase of etching time, the signals of organic components decrease slightly at 30 s and then maintain nearly constant throughout the subsequent depth profile. This stable distribution enables the formation of a flexible physical barrier, which can effectively suppress persistent side reactions between the electrolyte and Li anode. Meanwhile, the elevated LiF content in Fig. S28b is conducive to achieving the uniform lithium deposition. And no distinct –OH signals are detected in the O 1*s* spectra (Fig. S28c), verifying the interfacial stability of the PDA layer throughout cycling. These analyses demonstrate, again, that the PDA-gated interface facilitates the formation of a favorable SEI composed of flexible organic species and highly Li^+-conductive inorganic components. This interface ensures long-term, dendrite-free lithium deposition and stripping.

To gain electrochemical insight into interfacial stability, the EIS was conducted on symmetric Li cells over multiple cycles. The initial impedance of LLTO/GE is significantly higher than that of PDA_2@LLTO/GE (Figs. 5e and S29). Moreover, the Li| LLTO/GE |Li cell exhibits large impedance fluctuations during 20 cycles at 0.1 mA cm^{-2}. In contrast, the PDA_2@LLTO/GE-based cell maintains a lower and more stable impedance. To correlate the impedance response with specific interfacial processes, we analyzed the distribution of relaxation times (DRT). Three main contributions were identified (Fig. 5f, g): C1 at the high-frequency region ($\tau \approx 10^{-6}$ s), corresponding to bulk resistance (R_b); C2 and C3 at the mid-frequency regions ($\tau \approx 10^{-4}$ to 10^{-3} s), assigned to SEI impedance (R_{SEI}); C4 and C5 at the low-frequency regions ($\tau \approx 10^{-2}$ to 10^{-1} s), related to charge transfer impedance (R_{ct}). Compared to the Li| LLTO/GE |Li cell, PDA_2@LLTO/GE-based cell maintains low and stable R_{SEI} components (C2, C3) over 20 cycles (Fig. 5h, i), reflecting a robust and stable SEI layer. This stability supports consistent Li^+ transport and aligns with the steady overpotential observed during long-term cycling.

https://doi.org/10.1007/s40820-026-02127-6

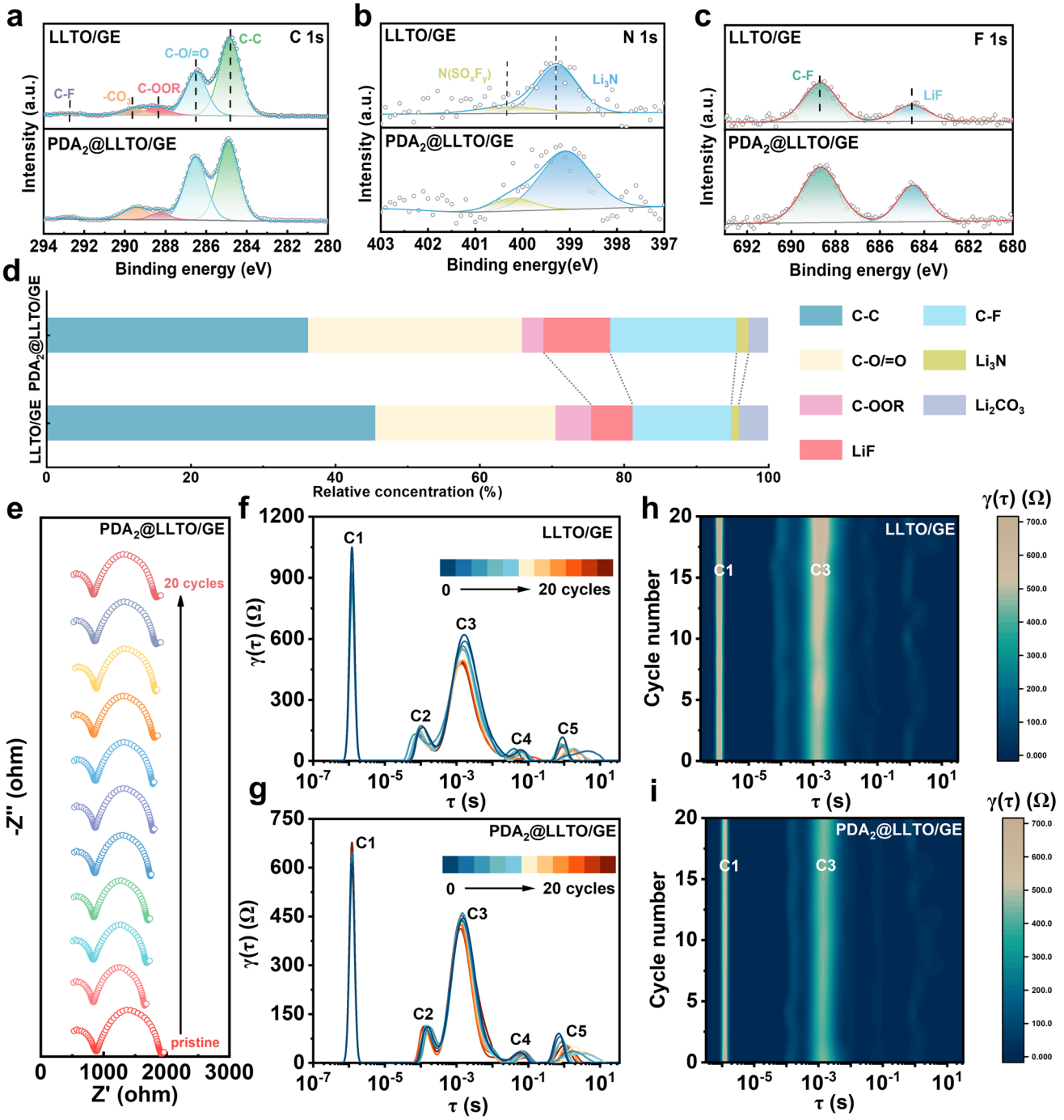

Fig. 5 Electrolyte–electrode interface electrochemical properties. **a-c** XPS spectra of the Li surface after 20 cycles with LLTO/GE and PDA_2@LLTO/GE electrolytes: **a** C 1*s*, **b** N 1*s*, and **c** F 1*s*. **d** Quantitative analysis of chemical components in the SEI layer for LLTO/GE and PDA_2@LLTO/GE. **e** EIS plots of Li | PDA_2@LLTO/GE | Li cell after different cycles. DRT analysis of **f, h** Li | LLTO/GE | Li and **g, i** Li | PDA_2@LLTO/GE | Li cells after various cycles at 0.1 mA cm^{-2}

3.4 Electrochemical Performance of Polyphenol-Gated CSEs in Li||LFP Full Battery

We then evaluated the performance of full batteries assembled with $LiFeO_4$ (LFP) cathode and PDA@LLTO/GE electrolyte at 60 °C. The LFP| PDA_2@LLTO/GE |Li cell delivers a high initial specific capacity of 151.6 mAh g^{-1} and retains 85.5% of its capacity after 600 cycles at 1 C, with Coulombic efficiency (CE) consistently above 99.5% (Fig. 6a). In contrast, the LFP| LLTO/GE |Li cell suffers from rapid capacity decay, with only 90 mAh g^{-1} remaining after the same period. Galvanostatic charge/discharge curves demonstrate stable cycling and low polarization for LFP| PDA_2@LLTO/GE |Li cells, with a capacity degradation rate of just 3.65% per cycle (Fig. 6b). Other PDA_x@LLTO/GE also outperform LLTO/GE electrolyte (Fig. S30). Besides, even assembled with a high LFP loading of 5 mg cm^{-2}, the PDA_2@LLTO/GE still retains a superior discharge capacity of 135.1 mAh g^{-1} with 84.7% capacity retention after 100 cycles at 1 C, while the capacity of LFP| LLTO/GE |Li has declined to 76.5 mAh g^{-1} (Fig. S31). Under high-rate conditions, LFP| PDA_2@LLTO/GE |Li cell achieves 125.7 mAh g^{-1} at 5 C, significantly higher than that of LLTO/GE cell (51.9 mAh g^{-1}) (Fig. 6c). This cell also exhibits lower polarization across various current densities (Figs. 6d and S32) and even after 1000 cycles at 5 C can sustain 80.7 mAh g^{-1}. By contrast, the LFP| LLTO/GE |Li cell declines from 93.0 mAh g^{-1} to just 43.2 mAh g^{-1} (Fig. S33a). Full cells coupled with PTA_2@LLTO/GE and PGA_2@LLTO/GE electrolytes also show high capacity retentions of 59% and 54%, respectively, after 1000 cycles (Fig. S33b). Compared with state-of-the-art CSEs such as silane coupling agents grafted LLZO/PEO and lithium phosphate modified LLZTO/PVDF [48–53], PDA_2@LLTO/GE electrolyte demonstrates superior electrochemical performance and extended life span (Fig. 6e). To further validate the high-voltage stability of PDA_2@LLTO/GE, NCM811||Li full cells were also assembled. As shown in Fig. S34, owing to the boosted ion conductivity and widened electrochemical window of PDA_2@LLTO/GE, the resultant full cell delivers a high discharge capacity of 177.3 mAh g^{-1} and CE of 97.5% at the first cycle at 1 C. In contrast, the NCM811|LLTO/GE|Li only achieves an initial specific capacity of 153.1 mAh g^{-1} with a low CE of 93.2%. After 100 cycles, the unmodified LLTO/GE-based cell suffers severe capacity decay with a residual capacity of merely 74.9 mAh g^{-1}, whereas the cell with PDA_2@LLTO/GE maintains a high capacity of 100.5 mAh g^{-1} accompanied by stable voltage polarization throughout cycling. Additionally, the composition of the cathode electrolyte interphase (CEI) layer formed on the NCM811 cathode after 20 cycles at 1 C was investigated via XPS spectra. As illustrated in Fig. S35a, in PDA_2@LLTO/GE, the organic component displays decreased signals after etching for 60 s, while the inorganic components (LiF and Li_2O) show a significant enhancement at the inner region. They are well-recognized for the low-energy barriers for Li^+ transport and can reduce the side reactions to stabilize the electrode–electrolyte interface (Fig. S35b, c). Therefore, the optimized CEI layer featuring with flexible organic outer layer and a robust LiF/Li_2O-enriched inorganic inner layer ensures fast Li^+ conduction and interfacial stability to achieve superior high-voltage durability and cycling performance. On the contrary, the sluggish ion transport in the LLTO/GE-based sample impairs the interfacial stability, which forms the CEI with more organic content derived from the decomposition of the polymer matrix (Fig. S35d) and insufficient LiF/Li_2O (Fig. S35e, f), thus triggering intensive voltage polarization and rapid capacity degradation.

To validate the practical applicability, a single layer pouch battery with PDA_2@LLTO/GE electrolyte was prepared. It exhibits a standard open-circuit voltage of 3.4 V and successfully powers an electronic console (Fig. 6f). This battery offers a high discharge capacity of 141.0 mAh g^{-1} with 82.9% retention after 400 cycles at 1 C (Fig. 6g). Impressively, the pouch battery continues to operate under harsh conditions such as folding, cutting, and puncturing without leakage or explosion (Fig. 6h-k). These findings demonstrate that the polyphenol-gated interface enables efficient cross-phase Li^+ transport and interfacial stability, offering a compelling route toward next-generation solid-state lithium-metal batteries.

4 Conclusions

In summary, we developed a polyphenol-gated CSE that mimics the cytomembrane consisting of channel proteins to suppress $TFSI^-$ mobility and boosts Li^+-selective transport across the polymer-ceramic interface. Compared to conventional CSEs, the optimized PDA_2@LLTO/GE demonstrated a higher ionic conductivity of 3.01×10^{-4} S cm^{-1} at 60 °C and transference number of 0.68. As a result, PDA_2@LLTO/GE enabled the stable cycling of the Li symmetric cell for

https://doi.org/10.1007/s40820-026-02127-6

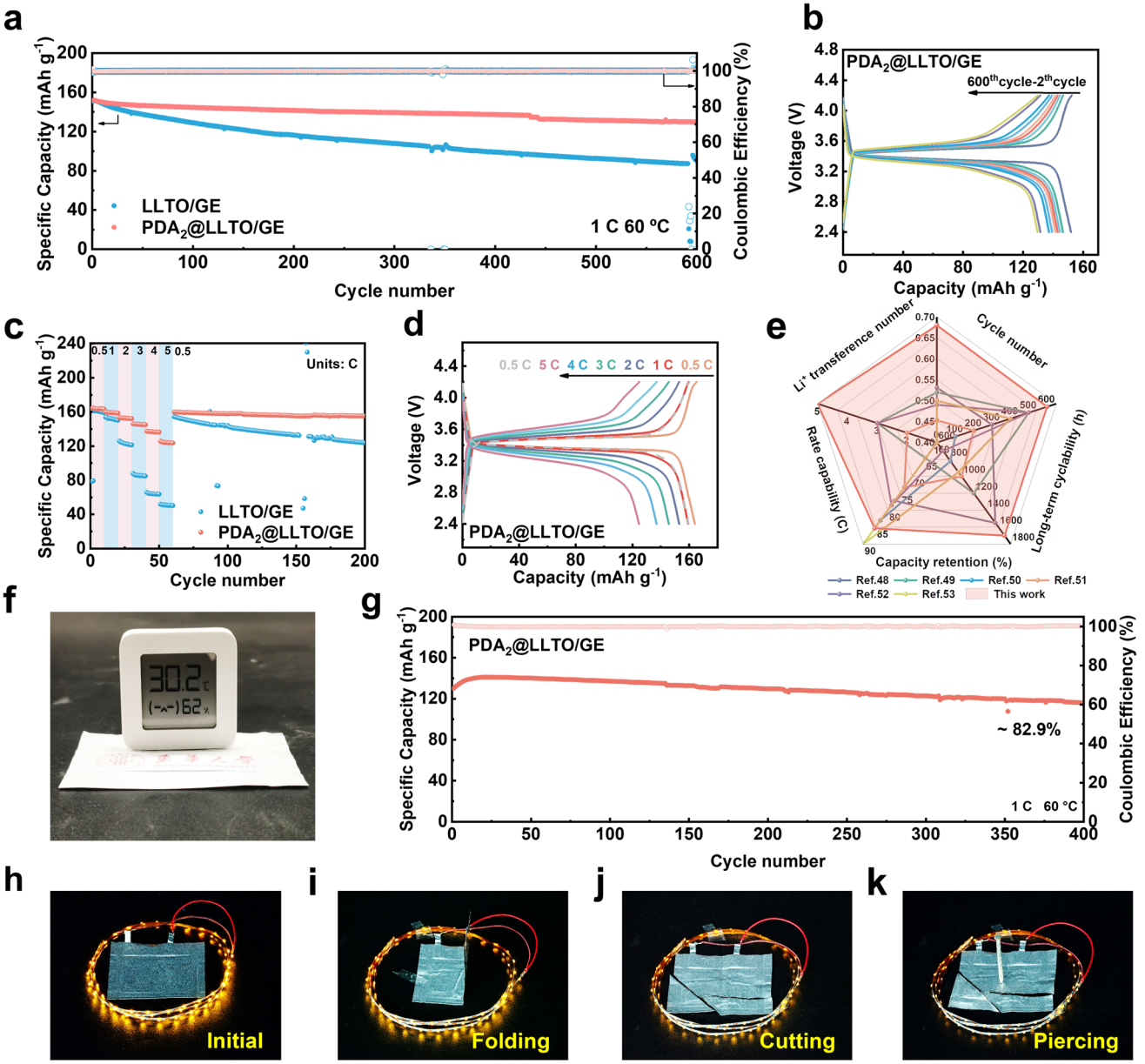

Fig. 6 Cycling performance of PDA_2@LLTO/GE electrolyte in $LiFePO_4$||Li full cells at 60 °C. **a** Long-term cycling performance of LFP| LLTO/GE |Li and LFP| PDA_2@LLTO/GE |Li full batteries at 1 C and 60 °C. **b** Charge/discharge profiles of LFP| PDA_2@LLTO/GE |Li cell. **c** Rate performance of full batteries. **d** Charge/discharge profiles of LFP| PDA_2@LLTO/GE |Li cell at 0.5—5 C. **e** Radar chart comparing electrochemical properties of different CSEs. **f** Digital image of LFP| PDA_2@LLTO/GE |Li pouch cell powering a hygrothermograph. **g** Long-term cycling stability of pouch cell fabricated with PDA_2@LLTO/GE at 1 C. **h–k** Safety tests of the pouch cell under folding, cutting, and piercing

over 1600 h and a high discharge capacity of 131 mAh g^{-1} for the LFP full cell even at 5 C. Furthermore, the pouch cell coupled with PDA_2@LLTO/GE exhibited excellent cycling performance with 82.9% retention after 400 cycles at 1 C. However, their long-term stability under thermal and electrochemical stress still requires further investigation. Expanding the molecular design to a broader range of robust polyphenols may enhance interfacial durability and optimize performance. Moreover, applying this concept to electrolyte–electrode interfaces could help to mitigate polarization and improve the high-rate cycling stability and compatibility between CSEs and high-voltage cathodes. Overall, this

work establishes a design concept for selective ion conduction across polymer-ceramic interfaces and provides new opportunities for the development of safer, longer-lasting solid-state lithium-metal batteries.

Acknowledgements This work was supported by the National Natural Science Foundation of China (Grants 52322302 and 22075042), the Shanghai Rising-Star Program (22QA1400300), Shanghai Scientific and Technological Innovation Project (22520710100), and the Fundamental Research Funds for the Central Universities (CUSF-DH-T-2024018). Y.Z. thanks funding from the European Union under the REFRESH-Research Excellence For REgion Sustainability and High-tech Industries project number CZ.10.03.01/00/22_003/0000048 via the Operational Programme Just Transition. The authors thank the Central Laboratory, the School of Chemical and Material Engineering, Jiangnan University, for their technical support.

Author Contributions Xiaoxiao Li contributed to conceptualization, investigation, methodology, data curation, formal analysis, visualization, and original draft writing. Minqiang Jiang, Kai Chen, and Zhixiang Cai were involved in investigation, formal analysis, and validation. Yingxin Zhang and Jiamei Luo helped in visualization and formal analysis. Lei Hou helped in software and methodology. Yazhou Zhou was involved in formal analysis, writing–review and editing, and funding acquisition. Chao Zhang and Hui Zhang contributed to formal analysis and resources. Feili Lai and Yue-E Miao worked in supervision, writing–review and editing, and funding acquisition. Tianxi Liu helped in resources and supervision. Klaus Müllen helped in conceptualization and writing–review and editing.

Declarations

Conflict of interest The authors declare no interest conflict. They have no known competing financial interests or personal relationships that could have appeared to influence the work reported in this paper.

Supplementary Information The online version contains supplementary material available at https://doi.org/10.1007/s40820-026-02127-6.

References

1. B. Liu, J.-G. Zhang, W. Xu, Advancing lithium metal batteries. Joule **2**(5), 833–845 (2018). https://doi.org/10.1016/j.joule.2018.03.008
2. Z. Zhang, W.-Q. Han, From liquid to solid-state lithium metal batteries: fundamental issues and recent developments. Nano-Micro Lett. **16**(1), 24 (2023). https://doi.org/10.1007/s40820-023-01234-y
3. Y. Qian, K. Chen, Z. Feng, Y. Ouyang, Q. Lan et al., A fluorinated-polyimide-based composite nanofibrous separator with homogenized pore size for wide-temperature lithium metal batteries. Small Struct. **4**(8), 2200383 (2023). https://doi.org/10.1002/sstr.202200383
4. X. Lu, Y. Wang, X. Xu, B. Yan, T. Wu et al., Polymer-based solid-state electrolytes for high-energy-density lithium-ion batteries–review. Adv. Energy Mater. **13**(38), 2301746 (2023). https://doi.org/10.1002/aenm.202301746
5. Y. Su, F. Xu, X. Zhang, Y. Qiu, H. Wang, Rational design of high-performance PEO/ceramic composite solid electrolytes for lithium metal batteries. Nano-Micro Lett. **15**(1), 82 (2023). https://doi.org/10.1007/s40820-023-01055-z
6. S. Zheng, Y. Chen, K. Chen, S. Yang, R. Bagherzadeh et al., *In situ* construction of polyether-based composite electrolyte with bi-phase ion conductivity and stable electrolyte/electrode interphase for solid-state lithium metal batteries. J. Mater. Chem. A **10**(37), 19641–19648 (2022). https://doi.org/10.1039/d2ta02229j
7. H. Liang, L. Wang, A. Wang, Y. Song, Y. Wu et al., Tailoring practically accessible polymer/inorganic composite electrolytes for all-solid-state lithium metal batteries: a review. Nano-Micro Lett. **15**(1), 42 (2023). https://doi.org/10.1007/s40820-022-00996-1
8. H. Xiang, L. Gao, D. Shi, L. Jiao, B. Cheng et al., Fast ion conductor nanofibers and aramid nanofibers with hydrogen bonds synergistically enhanced composite solid electrolytes. Adv. Fiber Mater. **6**(3), 883–899 (2024). https://doi.org/10.1007/s42765-024-00402-y
9. Y. Zheng, Y. Yao, J. Ou, M. Li, D. Luo et al., A review of composite solid-state electrolytes for lithium batteries: fundamentals, key materials and advanced structures. Chem. Soc. Rev. **49**(23), 8790–8839 (2020). https://doi.org/10.1039/d0cs00305k
10. K. Yang, L. Chen, J. Ma, C. Lai, Y. Huang et al., Stable interface chemistry and multiple ion transport of composite electrolyte contribute to ultra-long cycling solid-state $LiNi_{0.8}Co_{0.1}Mn_{0.1}O_2$/lithium metal batteries. Angew. Chem. Int. Ed. **60**(46), 24668–24675 (2021). https://doi.org/10.1002/anie.202110917
11. Z. Li, J. Fu, X. Zhou, S. Gui, L. Wei et al., Ionic conduction in polymer-based solid electrolytes. Adv. Sci. **10**(10), 2201718 (2023). https://doi.org/10.1002/advs.202201718
12. S. Lv, J. Wang, Y. Zhai, Y. Chen, J. Yang et al., Lithium-ion dynamic interface engineering of nano-charged composite polymer electrolytes for solid-state lithium-metal batteries.

Nano-Micro Lett. **18**(1), 46 (2025). https://doi.org/10.1007/s40820-025-01899-7

13. S. Lv, G. Wen, W. Cai, S. Yang, J. Yang et al., Building slippy ion-conduction highways in polymer electrolyte by electrostatic adsorption enabled asymmetric solvation structure. J. Energy Chem. **103**, 48–58 (2025). https://doi.org/10.1016/j.jechem.2024.11.050
14. S. Yuan, Z. Cao, Z. Zhao, S. Lv, Y. Zhai et al., An unchoked high-entropy composite electrolyte with Li^+-bond enabled tough-and-adhesive nano-interpenetrating network. Adv. Funct. Mater. **35**(43), 2503663 (2025). https://doi.org/10.1002/adfm.202503663
15. A. Xu, R. Wang, M. Yao, J. Cao, M. Li et al., Electrochemical properties of an Sn-doped LATP ceramic electrolyte and its derived sandwich-structured composite solid electrolyte. Nanomaterials **12**(12), 2082 (2022). https://doi.org/10.3390/nano12122082
16. L. Yang, Z. Wang, Y. Feng, R. Tan, Y. Zuo et al., Flexible composite solid electrolyte facilitating highly stable "soft contacting" Li–electrolyte interface for solid state lithium-ion batteries. Adv. Energy Mater. **7**(22), 1701437 (2017). https://doi.org/10.1002/aenm.201701437
17. B. Wang, G. Wang, P. He, L.-Z. Fan, Rational design of ultrathin composite solid-state electrolyte for high-performance lithium metal batteries. J. Membr. Sci. **642**, 119952 (2022). https://doi.org/10.1016/j.memsci.2021.119952
18. C. Yan, P. Zhu, H. Jia, Z. Du, J. Zhu et al., Garnet-rich composite solid electrolytes for dendrite-free, high-rate, solid-state lithium-metal batteries. Energy Storage Mater. **26**, 448–456 (2020). https://doi.org/10.1016/j.ensm.2019.11.018
19. X. Song, K. Ma, J. Wang, H. Wang, H. Xie et al., Three-dimensional metal–organic framework@Cellulose skeleton-reinforced composite polymer electrolyte for all-solid-state lithium metal battery. ACS Nano **18**(19), 12311–12324 (2024). https://doi.org/10.1021/acsnano.4c01257
20. H. Yang, J. Bright, B. Chen, P. Zheng, X. Gao et al., Chemical interaction and enhanced interfacial ion transport in a ceramic nanofiber–polymer composite electrolyte for all-solid-state lithium metal batteries. J. Mater. Chem. A **8**(15), 7261–7272 (2020). https://doi.org/10.1039/c9ta12495k
21. M. Liu, S. Zhang, E.R.H. van Eck, C. Wang, S. Ganapathy et al., Improving Li-ion interfacial transport in hybrid solid electrolytes. Nat. Nanotechnol. **17**(9), 959–967 (2022). https://doi.org/10.1038/s41565-022-01162-9
22. Z. Zhang, S. Zhang, S. Geng, S. Zhou, Z. Hu et al., Agglomeration-free composite solid electrolyte and enhanced cathode-electrolyte interphase kinetics for all-solid-state lithium metal batteries. Energy Storage Mater. **51**, 19–28 (2022). https://doi.org/10.1016/j.ensm.2022.06.025
23. L. Zhao, X. Yu, J. Jiao, X. Song, X. Cheng et al., Building cross-phase ion transport channels between ceramic and polymer for highly conductive composite solid-state electrolyte. Cell Rep. Phys. Sci. **4**(5), 101382 (2023). https://doi.org/10.1016/j.xcrp.2023.101382
24. W.-P. Chen, H. Duan, J.-L. Shi, Y. Qian, J. Wan et al., Bridging interparticle Li^+ conduction in a soft ceramic oxide electrolyte. J. Am. Chem. Soc. **143**(15), 5717–5726 (2021). https://doi.org/10.1021/jacs.0c12965
25. H. Yuan, W. Lin, C. Tian, M. Buga, T. Huang et al., Enhancement of Li^+ transport through intermediate phase in high-content inorganic composite quasi-solid-state electrolytes. Nano-Micro Lett. **17**(1), 288 (2025). https://doi.org/10.1007/s40820-025-01774-5
26. Z. Lu, L. Peng, Y. Rong, E. Wang, R. Shi et al., Enhanced electrochemical properties and optimized Li^+ transmission pathways of PEO/LLZTO-based composite electrolytes modified by supramolecular combination. Energy Environ. Mater. **7**, e12498 (2024). https://doi.org/10.1002/eem2.12498
27. S. An, E.J. Jeon, S.Y. Han, J. Jeon, M.J. Lee et al., pH-universal catechol-amine chemistry for versatile hyaluronic acid bioadhesives. Small **18**(41), 2202729 (2022). https://doi.org/10.1002/smll.202202729
28. L.Q. Xu, K.-G. Neoh, E.-T. Kang, Natural polyphenols as versatile platforms for material engineering and surface functionalization. Prog. Polym. Sci. **87**, 165–196 (2018). https://doi.org/10.1016/j.progpolymsci.2018.08.005
29. S. Chen, Y. Wu, S. Niu, Z. Wei, Y. Wu et al., Interface manipulation of composite solid polymer electrolyte with polydopamine to construct durable and fast Li^+ conduction pathways. ACS Appl. Energy Mater. **6**(3), 1989–2000 (2023). https://doi.org/10.1021/acsaem.2c03911
30. Z. Huang, W. Pang, P. Liang, Z. Jin, N. Grundish et al., A dopamine modified $Li_{6.4}La_3Zr_{1.4}Ta_{0.6}O_{12}$/PEO solid-state electrolyte: enhanced thermal and electrochemical properties. J. Mater. Chem. A **7**(27), 16425–16436 (2019). https://doi.org/10.1039/c9ta03395e
31. T.H. Mengesha, S.L. Beshahwured, Y.-S. Wu, S.-H. Wu, R. Jose et al., A polydopamine-modified garnet–based polymer-in-ceramic hybrid solid electrolyte membrane for high-safety lithium metal batteries. Chem. Eng. J. **452**, 139340 (2023). https://doi.org/10.1016/j.cej.2022.139340
32. X. Kan, C. Wu, L. Wen, L. Jiang, Biomimetic nanochannels: from fabrication principles to theoretical insights. Small Methods **6**(4), 2101255 (2022). https://doi.org/10.1002/smtd.202101255
33. Y. Zhang, X. Yu, X. Li, J. Ren, P. He et al., LLZTO crosslinks form a highly stretchable self-healing network for fast healable all-solid lithium metal batteries. Chem. Eng. J. **497**, 154397 (2024). https://doi.org/10.1016/j.cej.2024.154397
34. J. Bi, L. Zhang, B. Wu, M. Xiao, L. Wang et al., An LLTO-containing heterogeneous composite electrolyte with a stable interface for solid-state lithium metal batteries. Dalton Trans. **52**(39), 14064–14074 (2023). https://doi.org/10.1039/d3dt01677c
35. S. Chen, Z. Wei, C. Bai, S. Niu, W. Wei, Multiple intermolecular engineering of polymer electrolyte interphase by polyoxometalate-modified polydopamine filler for all-solid-state batteries. Chem. Eng. J. **472**, 145140 (2023). https://doi.org/10.1016/j.cej.2023.145140
36. X. Tian, S. Zou, R. Lv, J. Liu, B. Na et al., Well-dispersed polydopamine in situ coated lithium montmorillonite

nanofillers composite polyethylene oxide-based solid electrolyte for all-solid-state lithium batteries. Energy Technol. **12**(4), 2300980 (2024). https://doi.org/10.1002/ente.202300980

37. Q. Wang, T. Dong, Q. Zhou, Z. Cui, X. Shangguan et al., An *in-situ* generated composite solid-state electrolyte towards high-voltage lithium metal batteries. Sci. China Chem. **65**(5), 934–942 (2022). https://doi.org/10.1007/s11426-022-1221-4
38. J. Gai, F. Ma, Z. Zhang, D. Sun, Y. Jin et al., Flexible organic–inorganic composite solid electrolyte with asymmetric structure for room temperature solid-state Li-ion batteries. ACS Sustainable Chem. Eng. **7**(19), 15896–15903 (2019). https://doi.org/10.1021/acssuschemeng.9b01869
39. C. Li, S. Zhou, L. Dai, X. Zhou, B. Zhang et al., Porous polyamine/PEO composite solid electrolyte for high performance solid-state lithium metal batteries. J. Mater. Chem. A **9**(43), 24661–24669 (2021). https://doi.org/10.1039/D1TA04599G
40. Q. Ruan, M. Yao, J. Lu, Y. Wang, J. Kong et al., Mortise-tenon joints reinforced Janus composite solid-state electrolyte with fast kinetics for high-voltage lithium metal battery. Energy Storage Mater. **54**, 294–303 (2023). https://doi.org/10.1016/j.ensm.2022.10.037
41. M. Yao, Q. Ruan, S. Pan, H. Zhang, S. Zhang, An ultrathin asymmetric solid polymer electrolyte with intensified ion transport regulated by biomimetic channels enabling wide-temperature high-voltage lithium-metal battery. Adv. Energy Mater. **13**(12), 2203640 (2023). https://doi.org/10.1002/aenm.202203640
42. Z. Tian, L. Hou, D. Feng, Y. Jiao, P. Wu, Modulating the coordination environment of lithium bonds for high performance polymer electrolyte batteries. ACS Nano **17**(4), 3786–3796 (2023). https://doi.org/10.1021/acsnano.2c11734
43. W. Zhang, B. Wu, S. Sun, P. Wu, Skin-like mechanoresponsive self-healing ionic elastomer from supramolecular zwitterionic network. Nat. Commun. **12**, 4082 (2021). https://doi.org/10.1038/s41467-021-24382-4
44. I. Noda, Generalized two-dimensional correlation method applicable to infrared, Raman, and other types of spectroscopy. Appl. Spectrosc. **47**(9), 1329–1336 (1993). https://doi.org/10.1366/0003702934067694
45. K. Gong, L. Hou, P. Wu, Hydrogen-bonding affords sustainable plastics with ultrahigh robustness and water-assisted arbitrarily shape engineering. Adv. Mater. **34**(19), 2201065 (2022). https://doi.org/10.1002/adma.202201065
46. J. Li, Y. Cai, Y. Cui, H. Wu, H. Da et al., Fabrication of asymmetric bilayer solid-state electrolyte with boosted ion transport enabled by charge-rich space charge layer for-20~70 °C lithium metal battery. Nano Energy **95**, 107027 (2022). https://doi.org/10.1016/j.nanoen.2022.107027
47. H. Li, Y. Du, Q. Zhang, Y. Zhao, F. Lian, A single-ion conducting network as rationally coordinating polymer electrolyte for solid-state Li metal batteries. Adv. Energy Mater. **12**(13), 2103530 (2022). https://doi.org/10.1002/aenm.202103530
48. J. Xu, G. Ma, N. Wang, S. Zhao, J. Zhou, Borderline metal centers on nonporous metal-organic framework nanowire boost fast Li-ion interfacial transport of composite polymer electrolyte. Small **18**(40), 2204163 (2022). https://doi.org/10.1002/smll.202204163
49. X. Zheng, J. Wei, W. Lin, K. Ji, C. Wang et al., Bridging $Li_7La_3Zr_2O_{12}$ nanofibers with poly(ethylene oxide) by coordination bonds to enhance the cycling stability of all-solid-state lithium metal batteries. ACS Appl. Mater. Interfaces **14**(4), 5346–5354 (2022). https://doi.org/10.1021/acsami.1c21131
50. M. Jia, Z. Bi, C. Shi, N. Zhao, X. Guo, Polydopamine coated lithium lanthanum titanate in bilayer membrane electrolytes for solid lithium batteries. ACS Appl. Mater. Interfaces **12**(41), 46231–46238 (2020). https://doi.org/10.1021/acsami.0c14211
51. H. Chen, D. Adekoya, L. Hencz, J. Ma, S. Chen et al., Stable seamless interfaces and rapid ionic conductivity of Ca–CeO_2/LiTFSI/PEO composite electrolyte for high-rate and high-voltage all-solid-state battery. Adv. Energy Mater. **10**(21), 2000049 (2020). https://doi.org/10.1002/aenm.202000049
52. P. Pan, M. Zhang, Z. Cheng, L. Jiang, J. Mao et al., Garnet ceramic fabric-reinforced flexible composite solid electrolyte derived from silk template for safe and long-term stable all-solid-state lithium metal batteries. Energy Storage Mater. **47**, 279–287 (2022). https://doi.org/10.1016/j.ensm.2022.02.018
53. X. Yi, Y. Guo, S. Chi, S. Pan, C. Geng et al., Surface Li_2CO_3 mediated phosphorization enables compatible interfaces of composite polymer electrolyte for solid-state lithium batteries. Adv. Funct. Mater. **33**(35), 2303574 (2023). https://doi.org/10.1002/adfm.202303574

 https://doi.org/10.1007/s40820-026-02127-6